

Silicon nitride microwave photonic circuits

Chris G. H. Roeloffzen,^{1,2,*} Leimeng Zhuang,¹ Caterina Taddei,¹ Arne Leinse,³
René G. Heideman,³ Paulus W. L. van Dijk,² Ruud M. Oldenbeuving,²
David A. I. Marpaung,⁴ Maurizio Burla,⁵ and Klaus -J. Boller⁶

¹Telecommunication Engineering group, University of Twente, PO Box 217, Enschede, 7500 AE, the Netherlands

²SATRAX BV, PO Box 456, Enschede, 7500 AL, the Netherlands

³LioniX BV, PO Box 456, Enschede, 7500 AL, the Netherlands

⁴Centre for Ultrahigh Bandwidth Devices for Optical Systems (CUDOS), University of Sydney, Australia

⁵Institut National de la Recherche Scientifique (INRS-EMT), Montréal, Canada

⁶University of Twente, Laser Physics and Nonlinear Optics Group, MESA + Research Institute for Nanotechnology,
PO Box 217, 7500 AE, Enschede, the Netherlands

*c.g.h.roeloffzen@utwente.nl

Abstract: We present an overview of several microwave photonic processing functionalities based on combinations of Mach-Zehnder and ring resonator filters using the high index contrast silicon nitride (TriPleXTM) waveguide technology. All functionalities are built using the same basic building blocks, namely straight waveguides, phase tuning elements and directional couplers. We recall previously shown measurements on high spurious free dynamic range microwave photonic (MWP) link, ultra-wideband pulse generation, instantaneous frequency measurements, Hilbert transformers, microwave polarization networks and demonstrate new measurements and functionalities on a 16 channel optical beamforming network and modulation format transformer as well as an outlook on future microwave photonic platform integration, which will lead to a significantly reduced footprint and thereby enables the path to commercially viable MWP systems.

©2013 Optical Society of America

OCIS codes: (130.3120) Integrated optics devices; (060.5625) Radio frequency photonics; (070.6020) Continuous optical signal processing; (060.2360) Fiber optics links and subsystems; (350.4010) Microwaves.

References and links

1. J. Capmany and D. Novak, "Microwave photonics combines two worlds," *Nat. Photonics* **1**(6), 319–330 (2007).
2. J. Yao, "Microwave photonics," *J. Lightwave Technol.* **27**(3), 314–335 (2009).
3. D. A. I. Marpaung, C. G. H. Roeloffzen, R. G. Heideman, A. Leinse, S. Sales, and J. Capmany, "Integrated microwave photonics," *Laser Photon. Rev.* **7**(1), 1–33 (2013).
4. M. Burla, C. G. H. Roeloffzen, L. Zhuang, D. Marpaung, M. R. Khan, P. Maat, K. Dijkstra, A. Leinse, M. Hoekman, and R. Heideman, "System integration and radiation pattern measurements of a phased array antenna employing an integrated photonic beamformer for radio astronomy applications," *Appl. Opt.* **51**(7), 789–802 (2012).
5. M. Burla, D. Marpaung, L. Zhuang, A. Leinse, M. Hoekman, R. Heideman, and C. Roeloffzen, "Integrated photonic K_a-band beamformer chip with continuous amplitude and delay control," *IEEE Photon. Technol. Lett.* **25**(12), 1145–1148 (2013).
6. A. Meijerink, C. G. H. Roeloffzen, R. Meijerink, L. Zhuang, D. A. I. Marpaung, M. J. Bantum, M. Burla, J. Verpoorte, P. Jorna, A. Hulzinga, and W. C. van Etten, "Novel ring resonator-based integrated photonic beamformer for broadband phased-array antennas-Part I: design and performance analysis," *J. Lightwave Technol.* **28**(1), 3–18 (2010).
7. L. Zhuang, C. G. H. Roeloffzen, A. Meijerink, M. Burla, D. A. I. Marpaung, A. Leinse, M. Hoekman, R. G. Heideman, and W. C. van Etten, "Novel ring resonator-based integrated photonic beamformer for broadband phased-array antennas-Part II: experimental prototype," *J. Lightwave Technol.* **28**(1), 19–31 (2010).
8. L. Zhuang, C. G. H. Roeloffzen, R. G. Heideman, A. Borreman, A. Meijerink, and W. van Etten, "Single-chip ring resonator-based 1x8 optical beam forming network in CMOS-compatible waveguide technology," *IEEE Photon. Technol. Lett.* **19**(15), 1130–1132 (2007).

9. M. Burla, D. A. I. Marpaung, L. Zhuang, C. G. H. Roeloffzen, M. R. Khan, A. Leinse, M. Hoekman, and R. G. Heideman, "On-chip CMOS compatible reconfigurable optical delay line with separate carrier tuning for microwave photonic signal processing," *Opt. Express* **19**(22), 21475–21484 (2011).
10. L. Zhuang, D. A. I. Marpaung, M. Burla, W. P. Beeker, A. Leinse, and C. G. H. Roeloffzen, "Low-loss, high-index-contrast Si₃N₄/SiO₂ optical waveguides for optical delay lines in microwave photonics signal processing," *Opt. Express* **19**(23), 23162–23170 (2011).
11. D. Marpaung, C. Roeloffzen, A. Leinse, and M. Hoekman, "A photonic chip based frequency discriminator for a high performance microwave photonic link," *Opt. Express* **18**(26), 27359–27370 (2010).
12. D. A. I. Marpaung, L. Chevalier, M. Burla, and C. G. H. Roeloffzen, "Impulse radio ultrawideband pulse shaper based on a programmable photonic chip frequency discriminator," *Opt. Express* **19**(25), 24838–24848 (2011).
13. D. Marpaung, "On-chip photonic-assisted instantaneous microwave frequency measurement system," *IEEE Photon. Technol. Lett.* **25**(9), 837–840 (2013).
14. L. Zhuang, W. P. Beeker, A. Leinse, R. G. Heideman, P. van Dijk, and C. Roeloffzen, "Novel wideband microwave polarization network using a fully-reconfigurable photonic waveguide interleaver with a two-ring resonator-assisted asymmetric Mach-Zehnder structure," *Opt. Express* **21**(3), 3114–3124 (2013).
15. L. Zhuang, M. R. Khan, W. P. Beeker, A. Leinse, R. G. Heideman, and C. G. H. Roeloffzen, "Novel microwave photonic fractional Hilbert transformer using a ring resonator-based optical all-pass filter," *Opt. Express* **20**(24), 26499–26510 (2012).
16. C. K. Madsen and J. H. Zhao, *Optical Filter Design and Analysis: A Signal Processing Approach*. (Wiley-Interscience, 1999).
17. A. V. Oppenheim, and R. W. Schaffer, *Digital Signal Processing* (Prentice-Hall, 1975).
18. R. Adar, M. Serbin, and V. Mizrahi, "Less than 1 dB per meter propagation loss of silica waveguides measured using a ring resonator," *J. Lightwave Technol.* **12**(8), 1369–1372 (1994).
19. B. Larsen, L. Nielsen, K. Zenth, L. Leick, C. Laurent-Lund, L. Andersen, and K. Mattsson, "A low-loss, silicon-oxynitride process for compact optical devices," in *Proceedings of ECOC* (Rimini, Italy, 2003).
20. J. F. Bauters, M. J. R. Heck, D. John, D. Dai, M. C. Tien, J. S. Barton, A. Leinse, R. G. Heideman, D. J. Blumenthal, and J. E. Bowers, "Ultra-low-loss high-aspect-ratio Si₃N₄ waveguides," *Opt. Express* **19**(4), 3163–3174 (2011).
21. A. Melloni, R. Costa, G. Cusmai, and F. Morichetti, "The role of index contrast in dielectric optical waveguides," *Int. J. Mater. Prod. Technol.* **34**(4), 421–437 (2009).
22. F. Morichetti, A. Melloni, M. Martinelli, R. G. Heideman, A. Leinse, D. H. Geuzebroek, and A. Borreman, "Box-shaped dielectric waveguides: A new concept in integrated optics?" *J. Lightwave Technol.* **25**(9), 2579–2589 (2007).
23. M. Asghari, "Silicon Photonics: A low cost integration platform for datacom and telecom applications," in *Proc. OFC/NFOEC* (San Diego, Calif., USA, 2008).
24. R. G. Heideman, M. Hoekman, and F. Schreuder, "TriPleX™-based integrated optical ring resonators for lab-on-a-chip- and environmental detection," *IEEE J. Sel. Top. Quantum Electron.* **18**(5), 1583–1596 (2012).
25. A. Leinse, R. G. Heideman, M. Hoekman, F. Schreuder, F. Falke, C. G. H. Roeloffzen, L. Zhuang, M. Burla, D. Marpaung, D. H. Geuzebroek, R. Dekker, E. J. Klein, P. W. L. van Dijk, and R. M. Oldenbeuving, "TriPleX waveguide platform: low-loss technology over a wide wavelength range," *Proc. SPIE* **8767**, 87670E (2013), doi:10.1117/12.2020574.
26. R. M. Oldenbeuving, E. J. Klein, H. L. Offerhaus, C. J. Lee, H. Song, and K.-J. Boller, "25 kHz narrow spectral bandwidth of a wavelength tunable diode laser with a short waveguide-based external cavity," *Laser Phys. Lett.* **10**(1), 015804–015812 (2013).
27. M. Smit, J. Van der Tol, and M. Hill, "Moore's law in photonics," *Laser Photon. Rev.* **6**(1), 1–13 (2011).
28. C. Ciminelli, F. Dell'Olio, M. N. Armenise, F. M. Soares, and W. Passenberg, "High performance InP ring resonator for new generation monolithically integrated optical gyroscopes," *Opt. Express* **21**(1), 556–564 (2013).
29. M. Lysevych, H. H. Tan, F. Karouta, and C. Jagadish, "Single-step RIE fabrication process of low loss InP waveguide using CH₄/H₂ chemistry," *J. Electrochem. Soc.* **158**(3), H281–H284 (2011).
30. R. M. Oldenbeuving, "Spectral control of diode lasers using external waveguide circuits," PhD-thesis (Universiteit Twente, 2013).
31. Website of Eutelsat, a satellite operator, www.eutelsat.com/en/satellites/the-fleet/EUTELSAT-KA-SAT.html, visited May 28 2013.
32. S. R. Davis, G. Farca, S. D. Rommel, S. Johnson, and M. H. Anderson, "Liquid crystal waveguides: new devices enabled by > 1000 waves of optical phase control," *Proc. SPIE* **7618**, 76180E (2010).
33. D. Marpaung, L. Zhuang, M. Burla, C. Roeloffzen, J. Verpoorte, H. Schippers, A. Hulzinga, P. Jorna, W. P. Beeker, A. Leinse, R. Heideman, B. Noharet, Q. Wang, B. Sanadgol, and R. Baggen, "Towards a broadband and squint-free Ku-band phased array antenna system for airborne satellite communications," in *Proc. of the Fifth European Conference on Antennas and Propagation EuCAP* (Rome, Italy, 2011).
34. R. L. Moreira, J. Garcia, W. Li, J. Bauters, J. S. Barton, M. J. R. Heck, J. E. Bowers, and D. J. Blumenthal, "Integrated ultra-low-loss 4-bit tunable delay for broadband phased array antenna applications," *IEEE Photon. Technol. Lett.* **25**(12), 1165–1168 (2013).
35. W. Li, W. Zhang, and J. Yao, "An ultra-wideband 360° photonic-assisted microwave phase shifter," in *Proc. of OFC/NFOEC* (Anaheim, Calif., USA, 2013).

36. P. A. Morton and J. B. Khurgin, "Microwave photonic delay line with separate tuning of the optical carrier," *IEEE Photon. Technol. Lett.* **21**(22), 1686–1688 (2009).
 37. S. Chin, L. Thévenaz, J. Sancho, S. Sales, J. Capmany, P. Berger, J. Bourderionnet, and D. Dolfi, "Broadband true time delay for microwave signal processing, using slow light based on stimulated Brillouin scattering in optical fibers," *Opt. Express* **18**(21), 22599–22613 (2010).
 38. R. Won, "On-chip signal processing," *Nat. Photonics* **5**(12), 725 (2011), doi:10.1038/nphoton.2011.309.
-

1. Introduction

Microwave photonic (MWP) signal processing enables RF/microwave processing functionalities unreachable with conventional all-electronic signal processing solutions [1,2]. In integrated MWP the RF/microwave signals are first frequency up-converted to optical frequencies where they are processed in an optical chip. Exploiting the advantages inherent to integrated photonic devices, such as large instantaneous bandwidth, low loss transmission, easy implementation of tunability and re-configurability, electromagnetic inference insensitivity, as well as small size, low weight and power consumption. However, to become a disruptive technology to improve the mature RF/microwave electronics industry for both niche and consumer markets, MWP signal processing solutions still require effective reduction on the system cost, which is mostly limited by the use of non-integrated discrete optical devices. Its evolution is largely determined by the progress of on-chip MWP signal processing functionality [3].

Recently, a number of remarkable RF/microwave processing functionalities have been demonstrated using on-chip MWP signal processors, including tunable microwave filters, ultra-wideband microwave signal generation, tunable true time delay and beamforming, and high dynamic range MWP links. A comprehensive review of these functionalities can be found in [3]. Although these photonic integrated circuits (PICs) have been implemented in a number of different material platforms, such as indium phosphide, silicon, silica, or silicon nitride, a closer inspection shows that these PICs share the same key components. These are reconfigurable optical filters based on Mach-Zehnder Interferometers (MZIs) and optical ring resonators (ORRs). Implementation of MWP circuits in silicon nitride, in particular, has been very prolific in the past eight years, yielding various functions including optical beam forming [4–8], microwave phase shifters [9], microwave filters [10], MWP link [11], ultra-wideband signal generation [12], instantaneous frequency measurements [13], microwave polarization networks [14], and fractional Hilbert transformers [15]. This breadth of implementations is enabled by a particular silicon nitride platform, known as TriPleX™ waveguide technology, which features a very low propagation loss, compact bend radii, and a mature thermo-optical tuning scheme.

In this paper we present the key aspects of MWP signal processing in silicon nitride TriPleX™ waveguide platform. We will show that fairly high complexity, tunable MWP circuits for numerous MWP functionalities can be implemented using a set of standard building blocks, such as MZIs and ORRs, fabricated in this high performance waveguide technology. We briefly present the transfer functions of the elementary building block in its z -transform, highlight the key technological issues in the silicon nitride chip fabrication, and revisit the key functionalities achieved with these circuits. We will show the most recent MWP results, a 16×1 beamformer and a modulation format transformer, accomplished using this waveguide platform. Finally, we will discuss the prospect of these circuits for future MWP applications.

2. Theory

2.1 Microwave photonic link

A microwave photonic link is the workhorse of any MWP system. In order to obtain full functionalities from the MWP systems, the MWP link needs to reach sufficient performance. This is characterized by key performance indicators such as link gain, noise figure and

spurious free dynamic range (SFDR). The impact of signal losses is detrimental to these key metrics. One of the main challenges in designing an MWP link is to minimize signal losses arising from two sources: the one originating from the electrical-to-optical (E/O) and optical-to-electrical (O/E) conversions occurring at the modulators and the photodetectors, and the optical losses arising from component interconnections. It is imperative to minimize these optical losses since the relation between the RF loss and the optical loss in the MWP link is quadratic. The insertion of photonic integrated circuits in MWP systems is advantageous due to the promise of lower inter-component losses. But in turn, the overall insertion loss of the PICs should be minimized. This dictates the insertion of PICs with simultaneously low waveguide propagation loss and fiber-to-chip coupling loss [3].

2.2 Building blocks

The fundamental building blocks for realizing on chip microwave photonic functionalities in TriPleX™ waveguide technology are the optical waveguide, tuning element and directional coupler as shown in Table 1.

In order to obtain a framework for describing these building blocks and the more advanced variations to be discussed later, we will first introduce the concepts of the transfer matrix, the normalized frequency and the z-transform [16,17]. The overall transfer matrix of the MZI and ORR will be calculated in terms of the z-parameter.

Transfer matrix method and z-transform description of a waveguide

The transfer of a single mode waveguide (delay-section), as shown in Table 1(a) with a length L can be described as

$$H_{\text{wg}} = e^{-\alpha L} e^{-jk_0 n_{\text{eff}}(\omega)L} e^{-j\varphi} = \gamma e^{-j\omega\tau} e^{-j\varphi}, \quad (1)$$

where j is the imaginary unit, L is length of the waveguide, $k_0 = \omega/c$ is the vacuum wave number, ω the angular frequency of the guided wave, and c the speed of light in vacuum. The loss is given by $\gamma = \exp(-\alpha L)$, is the attenuation (loss in decibels: $A = -20\log|\gamma|$). In order to model, e.g., thermo-optic tuning, we do allow for a small deviation from the average effective index n_{eff} , leading to an additional tuning phase delay φ . The building block is shown in Table 1(b) and when required can be placed atop the waveguide. The group delay τ of this waveguide is given as

$$\tau = \frac{L \cdot n_g}{c}, \quad (2)$$

where n_g is the group index defined as

$$n_g = n_{\text{eff}}(\omega) + \omega \frac{\partial n_{\text{eff}}(\omega)}{\partial \omega}. \quad (3)$$

This delay-section has a periodic angular frequency response with period $\Delta\omega = 2\pi/\tau$ (or in temporal frequency $\Delta f = 1/\tau$)

In interferometric structures it is useful to normalize the angular frequency with respect to a fixed unit delay τ_u (with waveguide length L_u), so that the transfer function in terms of the normalized angular frequency $\omega' = \omega\tau_u$ (i.e. $f' = f\tau_u$) will be periodic with period $\Delta\omega' = 2\pi$ (i.e. $\Delta f' = 1$). In digital filter theory the so-called z-transform is widely used in order to simplify mathematics [17]. Then, by making the substitution

$$e^{-j\omega'} = z^{-1}, \quad (4)$$

the frequency transfer becomes a polynomial in z . Applying this z -transform, we arrive at the following transfer for a waveguide and tuning element

$$H_{wg} = \gamma z^{-1} e^{-j\phi}. \quad (5)$$

The transfer of a single waveguide can be extended to the matrix transfer of two parallel uncoupled waveguides with equal length as show in Table 1(c)

Group delay is a measure of linearity of the phase response with respect to the frequency. The group delay is the local slope of the phase response curve, i.e., the slope of the phase at the frequency being evaluated. A filter's group delay or envelope delay is defined as the negative derivative of the phase response with respect to angular frequency ω as follows [16]

$$\tau_g(\omega) = -\frac{d\theta(\omega)}{d\omega} = -\frac{d}{d\omega} \arg(H(z)) \Big|_{z=e^{j\omega}}. \quad (6)$$

The normalized group delay τ_g' is given in number of unit delays τ_u , leading to:

$$\tau_g'(\omega') = \frac{\tau_g}{\tau_u} = -\frac{d\theta(\omega')}{d\omega'} = -\frac{d}{d\omega'} \arg(H(z)) \Big|_{z=e^{j\omega'}}. \quad (7)$$

Directional coupler (2 × 2)

Couplers are among the most elementary building blocks in planar light wave circuits, performing the functions of splitting and combining guided optical waves. Directional couplers (DCs) consist of two optical waveguides in close proximity to each other, see Table 1(d). Light will be coupled by the evanescent field of the mode, and power will be exchanged between the waveguides. Arbitrary power splitting ratios can be obtained by simply choosing the length of the DC. The equation in the table gives a shorthand notation for the transfer matrix of a DC, where $c = (1 - \kappa)^{1/2}$ is the bar transfer function, and $-js = -j(\kappa)^{1/2}$ is the cross transfer function, and κ is the cross power coupling coefficient.


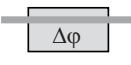
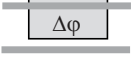
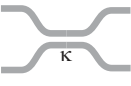
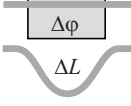

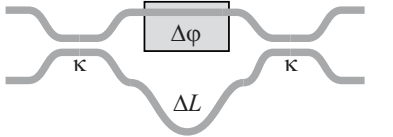
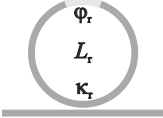
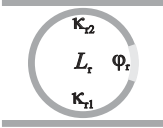
Differential delay section (two waveguides with different lengths) (2 × 2)

The delay section of an asymmetric MZI is formed by two independent waveguides having different lengths L_1 and L_2 respectively (we assume $L_2 > L_1$). The 2×2 port z -transfer is shown in Table 1(e) with upper branch as a reference. The differential loss $\gamma_{\Delta L} = \exp(-\alpha\Delta L)$ is the loss along the path length difference ΔL . The common length loss has been neglected in this equation. A tuning element has been placed on the upper waveguide.

Symmetric Mach-Zehnder Interferometer (2 × 2)

The symmetric MZI consists of two (assumed equal) DCs with power coupling ratios κ interconnected by two waveguides of equal length, where one can be phase tuned by the tuning element. The transfer matrix of the MZI, is shown in Table 1(f). The common path length has been neglected, since it adds only a constant loss and a linear phase to the frequency response. Since the power coupling of the MZI can be changed by tuning the phase of the tuning element it is a good candidate for a tunable coupling element.

Table 1. Basic building blocks and their transfer functions (back scattering, non-linearity's, common path lengths and non-idealities are neglected)

	Structure	Left	Layout	Right	Transfer
a	Waveguide (1×1)				$H_{wg} = \gamma z^{-1}$
b	Tuning element (1×1)				$H_{te} = e^{-j\varphi}$
c	two separate waveguides				$H_{2wg} = \begin{bmatrix} e^{-j\varphi} & 0 \\ 0 & 1 \end{bmatrix}$
d	Directional coupler (2×2)				$H_{dc} = \begin{bmatrix} c & -js \\ -js & c \end{bmatrix}$
e	Differential delay (2×2)				$H_{dd} = \begin{bmatrix} e^{-j\varphi} & 0 \\ 0 & \gamma_{\Delta L} z^{-1} \end{bmatrix}$
f	Symmetric MZI (2×2)				$H_{MZI} = \begin{bmatrix} -s^2 + c^2 e^{-j\varphi} & -jcs(1 + e^{-j\varphi}) \\ -jcs(1 + e^{-j\varphi}) & c^2 - s^2 e^{-j\varphi} \end{bmatrix}$
g	Asymmetric MZI (2×2)				$H_{AMZI} = \begin{bmatrix} -s^2 \gamma_{\Delta L} z^{-1} + c^2 e^{-j\varphi} & -jcs(e^{-j\varphi} + \gamma_{\Delta L} z^{-1}) \\ -jcs(e^{-j\varphi} + \gamma_{\Delta L} z^{-1}) & c^2 e^{-j\varphi} - s^2 \gamma_{\Delta L} z^{-1} \end{bmatrix}$
h	Ring resonator (1×1)				$H_r(z_r) = \frac{e^{-j\varphi_r} (c_r e^{+j\varphi_r} - \gamma_r z_r^{-1})}{1 - c_r e^{-j\varphi_r} \gamma_r z_r^{-1}}$
i	Ring resonator (2×2)				$H_T(z) = \frac{c_1 - c_2 \gamma z^{-1} e^{-j\varphi_r}}{1 - c_1 c_2 \gamma z^{-1} e^{-j\varphi_r}}$ $H_D(z) = \frac{-s_1 s_2 \sqrt{\gamma z^{-1} e^{-j\varphi_r}}}{1 - c_1 c_2 \gamma z^{-1} e^{-j\varphi_r}}$

Asymmetric Mach-Zehnder Interferometer (2 × 2)

The difference of the asymmetric Mach-Zehnder Interferometer (aMZI) as shown in Table 1(g) with respect to the symmetric MZI described above is the differential delay section, rendering its response frequency dependent. The bar and cross transfer are complementary sine-shaped functions. In terms of signal processing, such a device manifests a discrete-time finite impulse response. Figure 1(a) shows the frequency response of the aMZI filter for

several values of the differential loss. Note that the filter curve has a very narrow stopband having a bandwidth of only 4% of the free spectral range (FSR) at -25 dB suppression. Figure 1(b) shows the normalized group delay of the aMZI for different coupling constants, where the bell-shaped profile results from the fast phase change transition around the stopband center. Note that the ideal aMZI ($\kappa = 0.5 \rightarrow c = s = (0.5)^{1/2}$) has a constant group delay in the passband and thus allows dispersion-free transmission.

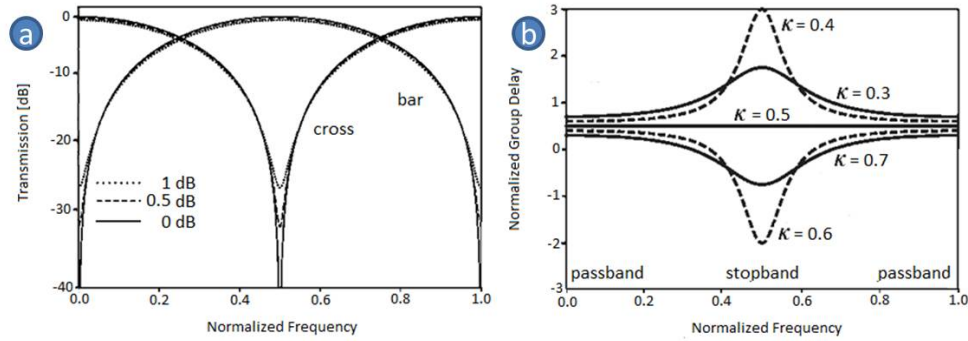


Fig. 1. (a) Magnitude response for the asymmetric Mach-Zehnder interferometer filter with differential loss of 0, 0.5 and 1 dB respectively. (b) Group delay transfer of the MZI for various coupling constants.

Ring resonator (1×1)

The waveguide implementation of a basic ring resonator (RR) with one input and one output is constructed by feeding one output of a 2×2 power coupler to the input of the same arm by means of a feedback loop (ring-shaped path). A schematic of this structure and the corresponding z-transform are given in Table 1(h). Inherent to the feedback mechanism, such a device is characterized by a discrete-time infinite impulse response [16]. Figure 2 depicts the frequency responses of a RR for different values of power coupling coefficient κ_r ($c_r = (1 - \kappa_r)^{1/2}$) and roundtrip loss P_L . Evidently, although the overall phase change over one FSR is a constant of 2π , the steepness of the phase change transition around the resonance frequency can be varied by changing κ_r . For the power transmission, the total loss of the device scales proportionally with the group delay and the waveguide propagation loss. Moreover, in practice, the resonance frequency of the device can be shifted by changing the additional roundtrip phase shift ϕ_r in the feedback loop.

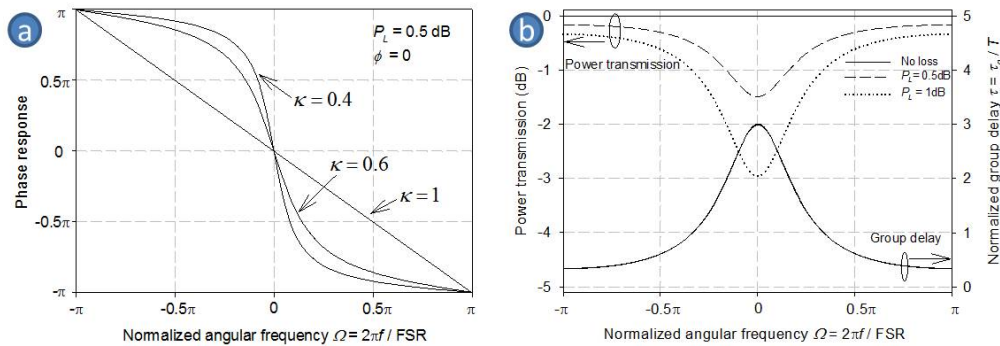


Fig. 2. Frequency responses of a ring resonator with one input and one output for different values of κ and P_L : (a) phase responses, (b) group delay and power transmissions.

Ring resonator (2×2)

The waveguide implementation of a ring resonator with two couplers, featuring two inputs and two outputs, is constructed using two times 2×2 couplers with one arm of a coupler joint to that of the other in a closed loop. A schematic of this structure and the corresponding z-transform are given in Table 1(i). Similar to MZIs, such devices also feature two power-complementary outputs and manifest better frequency selectivity inherent to the resonance mechanism. Hence, they are a good candidate for the add-drop functionality for wavelength (frequency) multiplexed signals. In addition to that, the sharp passband-stopband transition is also a useful property for many signal processing functionalities. The frequency responses of a ring resonator with two couplers are depicted in Fig. 3 for different setting of the coupling coefficients.

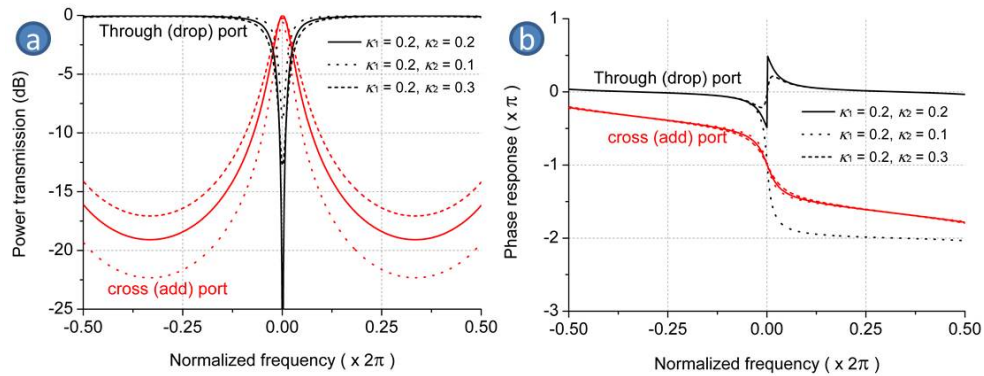


Fig. 3. Frequency responses of a ring resonator with two couplers for different settings of coupling coefficients: (a) power transmissions, (b) phase responses.

3. Chip realization (Technology)

To fabricate functional microwave photonic circuits in planar waveguide technology, multiple building blocks as described in Section 2 have to be connected in series or parallel. Such circuits have a typical footprint of several square centimeters [7,10]. In order to transmit optical signals with high enough power for easy detection through such a circuit, the optical propagation loss of the waveguides should be minimized. Previously, planar waveguides of different materials were realized with very low loss. As noticeable examples we mention waveguides with a core of phosphorus-doped silicon dioxide and silicon oxinitride, both with a low optical propagation loss of <0.05 dB/cm [18,19]. In general, waveguides that exhibit low propagation loss, also have a low refractive index contrast between core and cladding [20]. This can, e.g., be seen in the mentioned examples, where the refractive index contrasts are 0.6-0.7% and 2.5% respectively [18,19]. However, such low values of index contrast, via radiation loss, limit the waveguide's minimum bend radius. As a rule of thumb, the minimum bend radius in micrometer is given by $R_{min} = 5\Delta n^{-1.5}$, for 0.1 dB/rad radiation loss [21]. This causes the footprint of functional structures to be rather large. For the mentioned examples, the minimum bend radii were several millimeter. Therefore, a solution that optimizes this tradeoff, i.e., which provides a low loss and high index contrast, is preferred. Recently, silicon nitride waveguides with a silicon oxide cladding with a high index contrast (which can be tailored up to 20-30% [22]) have been shown to exhibit low optical loss (0.095 dB/cm), for small waveguide bend radii of $70 \mu\text{m}$ [10]. For the last-mentioned low optical loss measurements, the reader is referred to Section 4.2. The main contributor of optical propagation loss is scattering due to waveguide roughness [20]. By choosing the proper fabrication processes, waveguide roughness can be minimized. The latter mentioned results

were obtained in waveguides that were produced using a technology with minimized waveguide roughness, called Si₃N₄/SiO₂ TriPleX™ waveguide technology. In the following section the benefits of TriPleX™ technology, the fabrication process, possibilities and recent results are discussed.

The TriPleX™ waveguides described in this paper are fabricated using a Low Pressure Chemical Vapor Deposition (LPCVD) processes in which stoichiometric silicon nitride (Si₃N₄) and silicon oxide (SiO₂) are grown as superposing layers on a silicon wafer. The Si₃N₄ layers have a large tensile stress, whereas the SiO₂ layers have a large compressive stress, resulting in an overall low-stress layer stack. Using the LPCVD technique to deposit different layers has two main advantages. First it allows for thickness control on a nanometer scale, whereas the surface roughness is less than 0.4 nm, as measured by atomic force microscopy. This results in very low propagation losses, while maintaining high index contrast [20]. Secondly, it allows for mass-volume scaling because LPCVD is CMOS compatible [23].

TriPleX™ is usually fabricated in three different waveguide cross-sectional geometries, called box-shaped, double-stripe and single-stripe layout, as shown in Fig. 4. The fabrication steps (as adapted from Heideman *et al.* [24]) involved in the realization of each of these waveguide geometries are similar for a large part. All three types begin with a thermal oxidation of a 100 mm-diameter silicon wafer (Fig. 4, steps 1 and 2) to form the lower cladding. Then LPCVD Si₃N₄ (step 3) and tetraethylorthosilicate (TEOS) SiO₂ (step 4) are deposited. After a second deposition of LPCVD Si₃N₄ (step 5) - which is only required for the double-stripe-shaped geometry - the actual waveguide definition is performed by photolithography (step 6). This is followed by dry etching of the waveguide channels (step 7), with subsequent photo resist removal (step 8). For the box-shape geometry, then a third LPCVD Si₃N₄ (step 9) is deposited, followed by local removal of this slab nitride layer (step 10): without this local removal, the fabrication process is simplified but also leaves the optical circuitry with unwanted slab waveguiding effects. Then the top cladding SiO₂ layers can be applied, starting with a second TEOS oxide layer (step 11). A thick PECVD oxide layer is deposited (step 12), finalizing the waveguide structure.

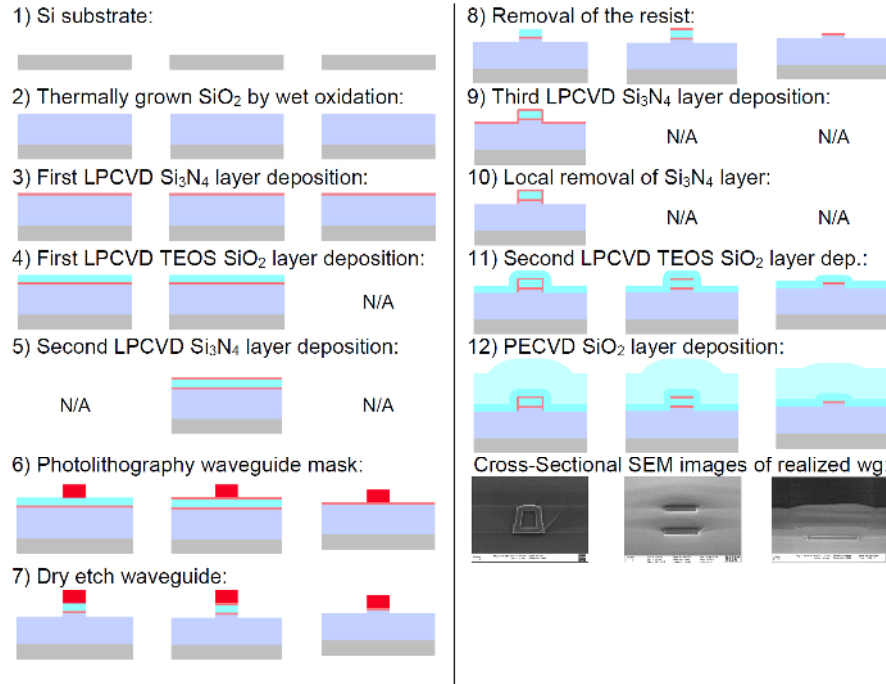


Fig. 4. Schematic cross-sectional view of a TriPleX process flow and corresponding SEM images of realized structures (bottom row) of three typical single-mode channel layouts: a box-shaped layout with minimal modal birefringence (left column), a double-stripe layout with strongly reduced modal birefringence (center column), and a single-stripe layout with large modal birefringence (right column). Legend of colors: --- = substrate, --- = bottom cladding, --- = waveguide, --- / --- = (different types of) cover layer. This figure is partially adapted from [24] and partially from [25].

To make microwave photonic circuits commercially viable, the conversion from RF signals to optical signals and back needs to be performed on-chip as well. This conversion is usually performed in active materials such as InP, for two main reasons. First, the speed in which InP can be addressed to modulate signals is orders of magnitude higher (GHz-range) than, e.g., in TriPleXTM (MHz-range [26]). Secondly, InP is an active waveguide material, so next to modulators, also lasers and detectors can be designed in InP [27]. For laboratory testing, discrete components of InP modulators, lasers and detectors are reliable and versatile. Nevertheless, for commercial mass-production purposes, discrete components are undesired. Luckily, complete arrays of lasers, modulators and detectors can be designed on the InP waveguide platform. However, InP waveguides have optical propagation losses many times higher than the previously discussed TriPleXTM waveguides [28,29]. Therefore hybrid integration between a low-loss waveguide platform like TriPleXTM and an active waveguide platform like InP seems advantageous. To couple these two platforms together with low insertion loss, the mode field diameters of the waveguides need to match at the interfaces. This can easily be done by tapering the TriPleXTM waveguides [24,25]. As example we mention a recent achievement [30], where an entire array of 49 diode lasers, with each diode specified to 1 Watt output power, was coupled to an array of tapered TriPleXTM waveguides with a single-stripe cross-section. The total loss (including residual mode mismatch, waveguide loss, misalignment, etc.) was measured to be reduced to only 2.2 dB. Additionally, a recent achievement of coupling an InP laser to an external cavity fabricated in a TriPleXTM chip with a box-shaped cross-section, resulted in an extremely narrow laser bandwidth of 25 kHz [26]. Here, the output of the laser was on the TriPleXTM chip, which is beneficial for further microwave photonic processing.

An important issue for commercial microwave photonic circuits is power consumption. As example, let us consider an 8×1 optical beam forming network (OBFN) as described by Zhuang *et al.* [7]. The fabricated circuits are optically tuned by means of refractive index changes induced by local heating. A tuning element capable of performing such local heating, has a typical average power consumption of about 350 mW. A π phase tuning is required on average. For a heater length of 2 mm the change in temperature underneath is approximately 40°C . The chip needs to be temperature stabilized within 0.1°C for stable operation of the RRs and MZIs. So for the described 8×1 OBFN, to which 8 antennas can be connected for conversion into a single output beam with tunable direction, the total power consumption is only several Watts. However, for functional designs in, e.g., satellites, many more beams and many more antennas are required. To give an example, the KaSat launched in 2010 [31], has a total number of 1900 antenna elements, and is capable of producing 82 separate beams. This means that if an OBFN as mentioned above would be used as beam forming network, the total power consumption for the heaters alone would be in the order of kilowatts to megawatts. Obviously, for use in a satellite this is too high. However, a recent publication [32], on the use of liquid crystal as top cladding for TriPleXTM waveguides has shown a dramatic decrease in power consumption per tuning element. By applying a voltage of only 5 V to the liquid crystal cladding, the refractive index of the waveguide is changed accordingly. This achieved similar tuning as attained with the above mentioned heaters, however with a dramatically lower power consumption by a factor of 80.000. This means that for future application of OBFNs in highly complex, high performance systems such as, e.g., satellite communication systems, the OBFN has to be equipped with a liquid crystal top cladding.

4. Chip characterization

4.1 Measurement setup

The experimental setup depicted in Fig. 5 is used to fully characterize the frequency responses of the components on the chip. When RF frequency sweeping and single-sideband full-carrier modulation to a CW light is performed (e.g., by using dual-parallel Mach-Zehnder modulator), this setup functions as an optical vector analyzer, which measures the amplitude and phase responses over the bandwidth allowed by the network analyzer. Besides, it can also be used to perform the direct group delay measurement using the well-known phase-shift method, where laser frequency sweeping and a fixed low frequency RF are employed instead and the measurement bandwidth is only determined by the frequency sweeping range of the laser. Moreover, the reconfiguration of the chips under test are performed by applying proper DC voltages to the tuning elements (heaters) on the chip. In practice, a dedicated channel-scalable control subsystem is preferred for characterization efficiency and setup complexity, especially when a large number of tuning elements are designed on the chip to support complex functionalities.

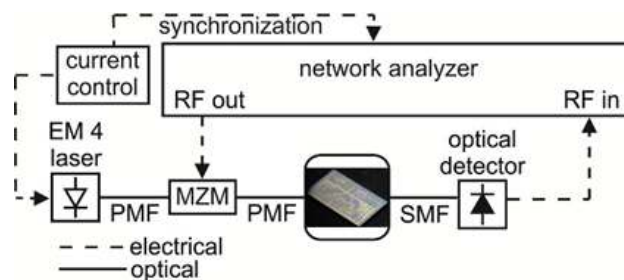


Fig. 5. Measurement setup for the characterizations of the fabricated optical chips. MZM is Mach-Zehnder modulator, PMF is polarization maintaining fiber, SMF is single mode fiber.

The RF frequency modulating the optical carrier can be adjusted according to the spectral resolution requirement (minimum 10 MHz with the used network analyzer).

A dedicated 12-bit control subsystem was used to drive the heaters on the chip, where the control information for each tuning element is read from a custom generated lookup table. Owing to the properties of the used waveguide (Si_3N_4) and heater material (chromium) issues regarding to drift are not observed.

4.2 Measurements of common PIC functionalities

Waveguide

In terms of PICs, the systematic propagation loss is the most important performance metric of a waveguide-based device. For the TriPleX™ waveguide geometry described in Section 3, the waveguide propagation loss has been characterized in a group of ring resonator-based delay lines, which are the most common building block of PICs. For the sake of comparison, the delay lines were fabricated with a common ring circumference of 8783 μm (corresponding to a FSR of 20 GHz) and ring-loop bend radii varying from 50 μm to 125 μm [10]. The device layout is depicted in Fig. 6(a), where the power coupler is implemented using an MZI coupler equipped with coupling-coefficient tunability by means of resistor-based heaters. The measurement results are depicted in Fig. 6(b). As shown in the result, the maximum system propagation loss was measured to be 0.12 dB/cm in the ORR with a bend radius of 50 μm , and an average waveguide propagation loss as low as 0.095 dB/cm was achieved for the bend radii ≥ 70 μm where the loss contribution of the bend radiation is negligible compared to the scattering loss of the waveguide. Besides, the small measurement deviations of the different devices also indicate good fabrication uniformity.

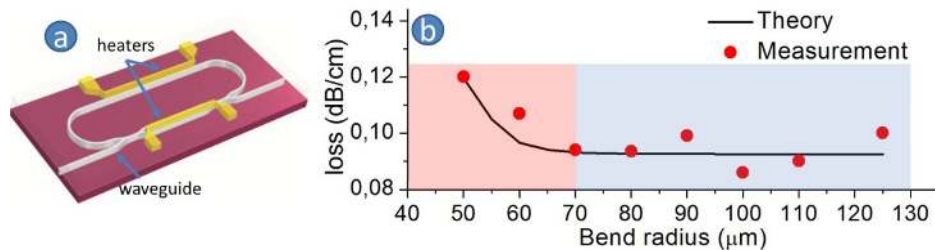


Fig. 6. (a) device layout and (b) measured systematic propagation loss of ring resonator-based delay lines in TriPleX™ technology (from [10]).

Arbitrary splitters and combiners

Two most fundamental and also critical PIC functionalities are the arbitrary splitter and combiner. In practice, both can be implemented using 2×2 MZI-based tunable couplers [7]. Beside the tunability in splitting/combining ratio, such MZI-based couplers can also be concatenated to construct binary-tree splitting/combining circuits, which features easy scalability. Figure 7(a) depicts the schematic of a 4×1 combiner constructed using three 2×2 MZI-based tunable couplers in a binary tree configuration, and Fig. 7(b) demonstrates the combining functionality of the device. For this demonstration, a CW laser was externally modulated by a RF signal with frequency range of 1 to 2 GHz, and subsequently split into four equal portions. Mutually synchronized, the four splits were applied to the four inputs of the device, where all the MZI-based couplers are set to 50/50 status. In agreement with the theory, the combining of every two inputs results in a 6 dB enhancement of the detected signals. Besides, background ripples exhibit in the measurement results, which are mainly due to the Fabry-Perot effect caused by the light reflections at the waveguide facets. However, this can be effectively reduced by optimizing the waveguide design.

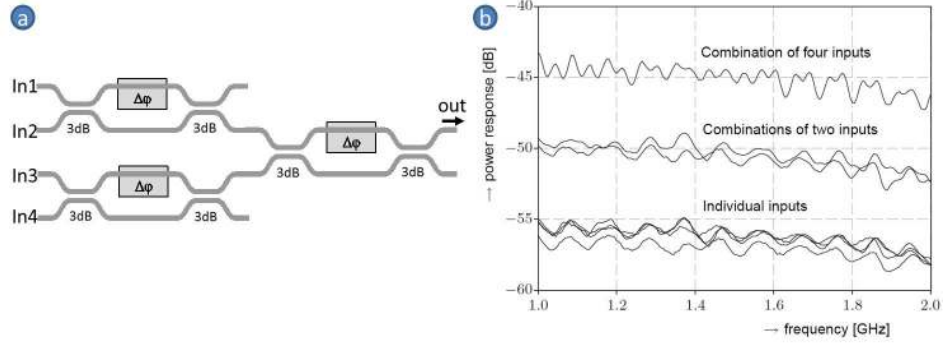


Fig. 7. (a) schematic and (b) measurements of a 4×1 combiner constructed using three times 2×2 MZI-based tunable couplers, where modulated optical signals with equal amplitude and synchronized phase are applied to the four inputs, and all the couplers are set to 50/50 status (from [7]).

Tunable delay lines

Tunable delay lines can be implemented using fully-programmable RRs, namely, equipped with tunability in both coupling coefficient and additional roundtrip phase shift [8]. When using multiple RRs in cascade configurations, the maximum delay line bandwidth for a certain target delay value increases approximately in linear relation with the number of RRs. Besides, inherent to the linear system properties, a larger delay can be achieved by means of adding up multiple smaller delays which are generated by separate delay lines in a serial cascade. When this delay functionality is incorporated in a binary-tree architecture, simultaneous generation of incremental delays can be realized. Figure 8 depicts a schematic of such a circuit with a 1×8 port configuration and RRs with a FSR of 14 GHz.

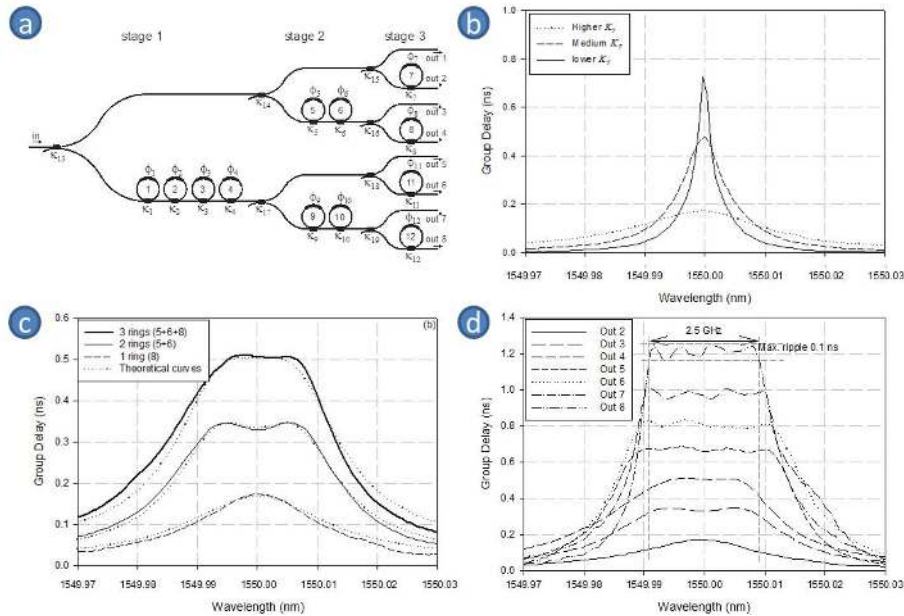


Fig. 8. (a) schematic of a delay line circuit with a 1×8 port configuration, (b)-(d) measured group delay responses of different output ports, where the ring resonators (RRs) are set such that incremental delays of different ports are aligned to a common center frequency (from [8]).

5. Construction of complex MWP signal processors

5.1 On-chip 16×1 optical beam former

Employing the proven PIC functionalities previously constructed, and using the waveguide basic building blocks, an example of complex, on-chip MWP signal processors, namely an optical beamformer chip for K_u -band phased array antennas [33] has been designed and fabricated. The full functionalities of such an optical beamformer chip have been elaborated on in [6,7], where an optical sideband filter (OSBF) and an optical carrier reinsertion coupler are incorporated together with the primary signal-combining circuit using RR-based delay lines. The intention is to apply the optical beam former in a K_u -band phased array antenna system to enable mobile broadband satellite communications. The chip is required to support 16 inputs, 4.5 GHz optical bandwidth, and a maximum delay of 290 ps. Correspondingly, this is translated into a functional design which consists of a 16×1 binary-tree combining circuit inserted symmetrically with a total of 40 RR-based delay lines, an OSBF using the MZI-double-RR architecture, and a flexible optical carrier reinsertion circuit allowing the optical carrier to be inserted from both sides of the chip. The schematic of the beam former architecture is depicted in Fig. 9(a), which is the most complex on-chip MWP signal processor to date. Using the waveguide bend radius of $125 \mu\text{m}$, a chip mask layout has been generated as shown in Fig. 9(b), which has a footprint as small as $0.7 \times 2.2 \text{ cm}$. Figure 9(c)-9(d) exhibit the photos of a processed wafer and a packaged chip, respectively.

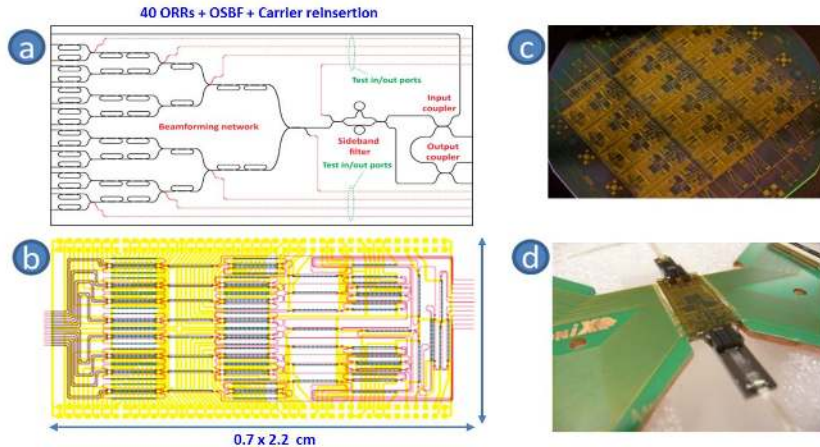


Fig. 9. (a) schematic of the designed 16×1 optical beamforming network (OBFN) chip; (b) chip mask layout using waveguide bend radius of $125 \mu\text{m}$; (c) a photo of a processed wafer; (d) a photo of a packaged chip with electrical connections and fiber pigtailling.

Several measurements have been performed on the fabricated 16×1 beamformer chip to verify the delay functionality. The used delay line configurations are shown in Fig. 10 together with the measured group delay responses over one FSR of 25 GHz. By using the tunable elements of each RR, i.e., a coupler and a phase shifter, different delays were obtained over a defined bandwidth. As shown in the results, the delay dynamic tuning range scales with the number of RRs in the cascade. For a cascade of 6 RRs, a maximum delay of 650 ps is achieved for a bandwidth of 4.5 GHz, which is in good agreement with the functional design.

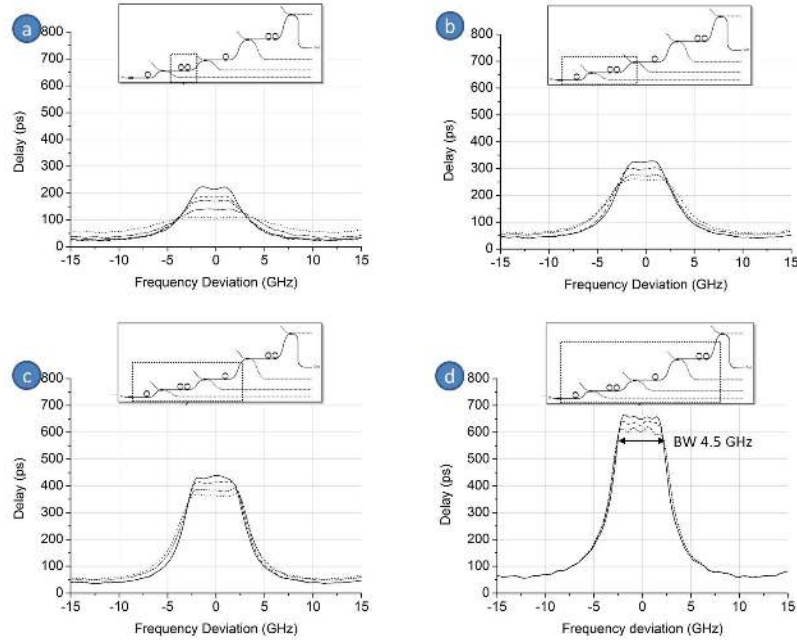


Fig. 10. Measured group delay responses of a cascade of (a) 2 RRs, (b) 3 RRs, (c) 4 RRs and (d) 6 RRs

5.2 Integrated phase-shifter and true-time-delay on a single chip based on separate carrier tuning

Tunable delay lines and phase shifters have a primary role in the implementation of multiple signal processing functionalities. The realization of continuously tunable delays with large tuning range (in the order of nanoseconds) and broadband performance (tens to hundreds of GHz) is highly desired for a number of functionalities, for example the realization of reconfigurable and highly selective microwave photonic filters, or for control of broadband phased array antennas. Several optical solutions have been proposed over the years to overcome the limited performance of purely-electronic true time delay (TTD) and phase shifting (PS), allowing to increase the amount of delay (almost 13 ns demonstrated in [34]) with bandwidths of hundreds of GHz and continuous tunability, and phase shifters with full- 360° tunability in mm-wave band [35]. In [9] we have shown a broadband (1 GHz) processor that includes delaying, phase shifting and single sideband filtering functionalities in a single unit. The delay module is based on the separate carrier tuning technique [36,37]. The processor consists of a reconfigurable optical delay line, a separate carrier tuning unit and an optical sideband filter. The optical sideband filter is an MZI with an optical ring resonator in one of its arms (Fig. 11, top). This filter is used to remove one of the RF sidebands of a double sideband plus carrier (DSB + C) signal previously generated using a Mach-Zehnder intensity modulator. Optical delay and carrier tuning are implemented using a pair of cascaded optical ring resonators each (Fig. 11, bottom). The group delay can be varied between 0 and approx. 400 ps by tuning the coupling factor of the optical ring resonators of the delay line, while simultaneously applying a full $0 - 360^\circ$ phase shift to the carrier using the carrier tuning unit (Fig. 12).

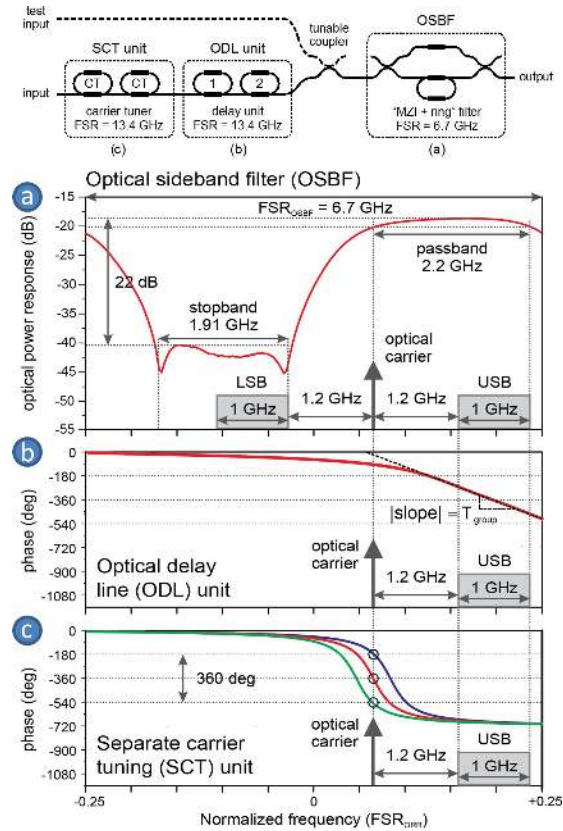


Fig. 11. Schematic layout of the separate carrier tuning (SCT) unit (top) and principle of operation (bottom) (from [9]).

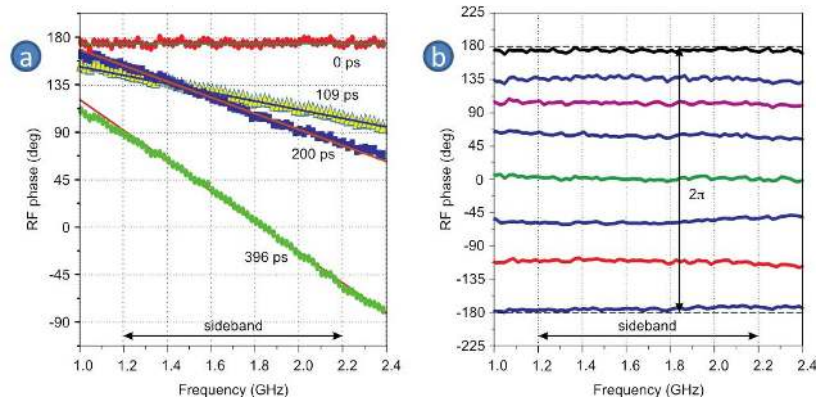


Fig. 12. Generation of tunable group delay (a) and of full-360° phase shift (b) using the integrated photonic processor (from [9]).

5.3 Microwave photonics filters

The principle of separate carrier tuning described in the previous section has been employed to demonstrate the capability to implement microwave photonic filters (MPFs) with complex coefficients of arbitrary complexity. In [9] we have shown the demonstration of a two-tap MPF where both notch position and FSR can be fully adjusted over a bandwidth of 1 GHz [38] (Fig. 14). The schematic is shown in Fig. 13.

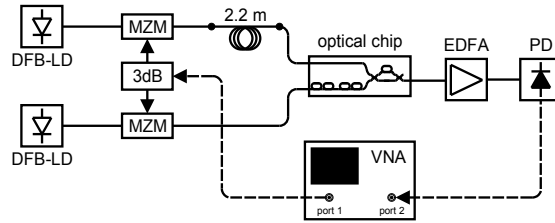


Fig. 13. Schematic of the microwave photonics filter (MPF) based on separate carrier tuning (SCT) (from [9]).

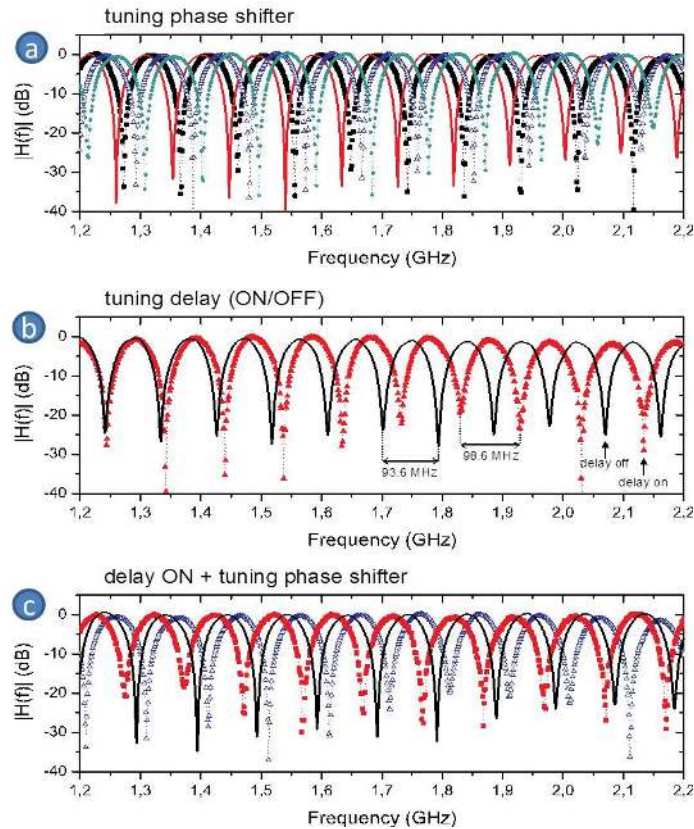


Fig. 14. Demonstration of the full tunability of the microwave photonics filter (MPF) based on separate carrier tuning (SCT). (a) shift of the resonance frequency. (b) Tuning of the FSR. (c) Simultaneous tuning of notch frequency and FSR (from [9]).

5.4 Spectral filters based on RR-assisted MZI architectures

Spectral filters are a widely required functionality for signal processing. Various well-known digital filter concepts can be implemented on-chip using waveguide analogies. For example, Chebyshev II filters featuring flat passband and sharp transition band are good candidates for optical sideband filtering. A practical way to construct this type of filter is to use RR-assisted MZI architectures [14]. Figure 15(a) depicts the schematics of waveguide implementations of 3rd-order and 5th-order Chebyshev II filters which use MZI-single-RR and MZI-double-RR architectures, respectively. The fabricated devices are characterized by a FSR of 19.6 GHz, and the filter coefficients are reconfigurable by means of the heaters. The optimized filter transmissions are depicted in Fig. 15(b), where the transition band improvement by increasing the filter order is demonstrated. Moreover, the measured complementary outputs, phase and

group delay responses of the MZI-double-RR filter are also depicted in Fig. 15(c)-15(e) in contrast with the simulations, which verify the device functionality and design accuracy.

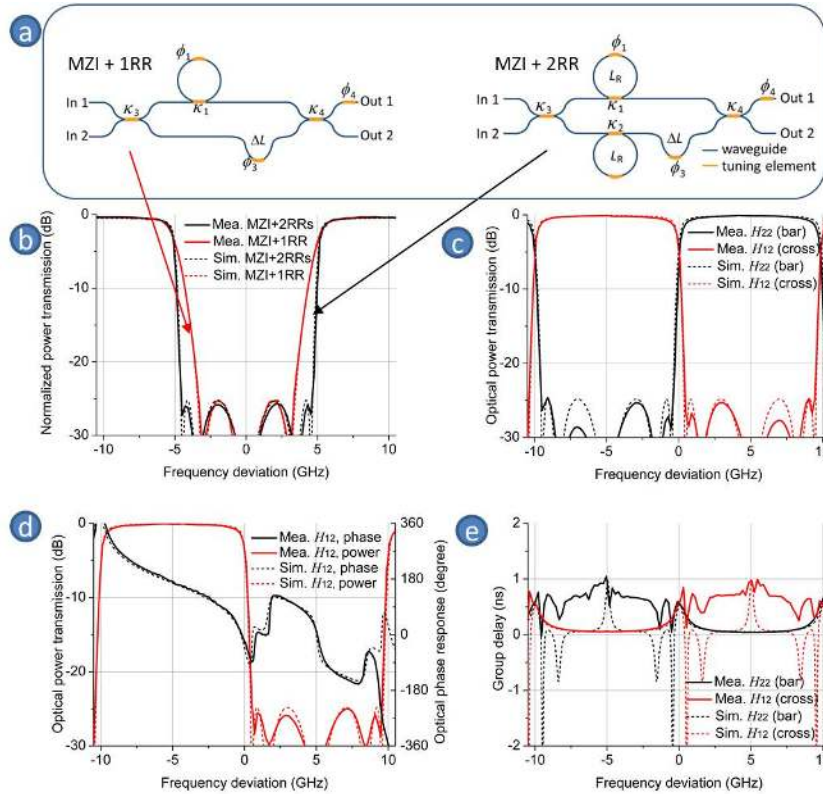


Fig. 15. (a) Schematics of waveguide implementations of 3-order and 5-order Chebyshev II filters using MZI-single-RR and MZI-double-RR architecture, respectively. (b) Comparison between the optimized filter transmissions. (c)-(d) Measured complementary outputs, phase and group delay responses of the MZI-double-RR filter (from [14] and [10]).

5.5 Frequency discriminator chip

Another example of an MWP circuit in TriPlexTM technology using the basic building blocks described above is the frequency discriminator chip depicted in Fig. 16. The chip consisted of five tunable 2×2 (i.e. add-drop) ring resonators [11] with two different FSRs: 21.5 GHz for Ring 1-3 and 10.7 GHz for Ring 4 and 5. The chip was implemented using the box-shaped TriPlexTM waveguides with a bend radius of 150 μm . The chip footprint measured to be 9 mm \times 7 mm. This chip has been designed to efficiently convert phased modulation signals into intensity modulation (i.e. frequency discrimination). Three different applications have been demonstrated using this chip, namely high spurious-free dynamic range (SFDR) MWP link [11], ultra-wideband pulse generation [12], and instantaneous frequency measurement [13].

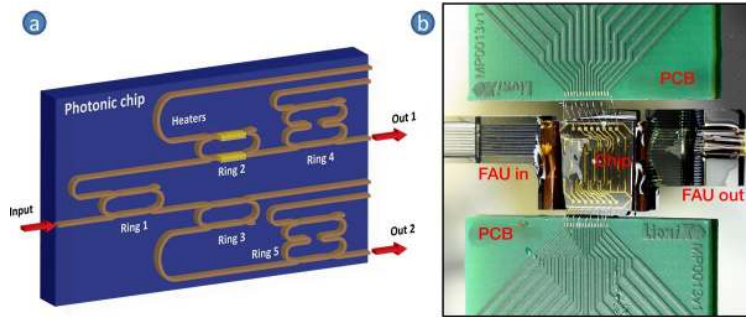


Fig. 16. (a) Layout of the frequency discriminator chip; (b) the realization (right) (from [11]).

5.5.1 High SFDR MWP link

Most applications of MWP systems such as antenna beam forming and antenna remoting demand a high dynamic range. For this reason, a lot of effort has been directed towards suppressing the noise and nonlinear distortions in MWP links, the two main factors limiting the SFDR. Studies have shown that phase modulation is a promising technique in SFDR enhancement compared to its intensity modulation counterpart. The frequency discriminator in Fig. 16 was designed to convert phase modulation (PM) to intensity modulation (IM) with reduced nonlinear distortions, thereby harnessing the linearity of PM while preserving the ease of direct detection attributed to IM. Here, a cascade of responses from through ports of ORRs (for example Ring 2 and 4) is used to linearize the response from drop port of another ORR (for example Ring 1). This optical response is then used to convert PM to IM. The chip programmability, combined with the balanced detection scheme, allowed the synthesis of a linear response from the complementary chip outputs. The optimized response exhibited a region where maximized signal power occurred when both second-order and third-order intermodulation distortions were minimized (Fig. 17(a)). At this particular configuration, the MWP link exhibited an improved second-order and third-order SFDRs (Fig. 17(b)).

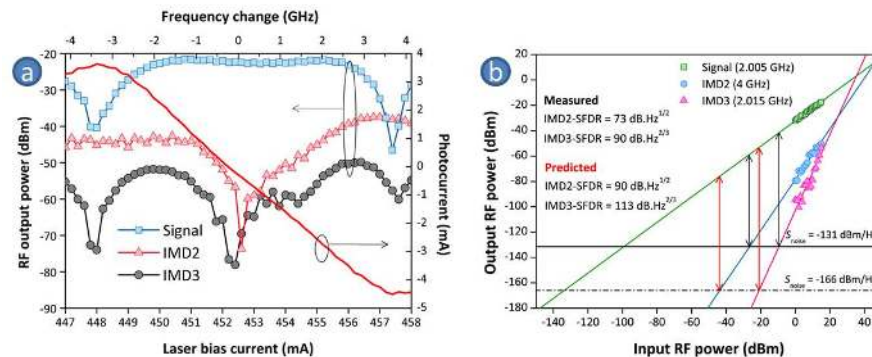


Fig. 17. (a) Two tone test measurement results depicting signal and intermodulation distortion (IMD) powers and the photocurrent as functions of the laser bias current for a balanced response from Ring 1, 3 and 5. (b) The measured spurious-free dynamic range (SFDR) for the balanced response. (from [11]).

5.6 Ultrawideband pulse generation

Ultra-wideband (UWB) signal generation is one of the key applications of MWP, because it clearly highlights the advantage of wide bandwidth of photonics. Flexible generation and spectrum shaping of RF pulses with multiple-gigahertz bandwidth has been proven challenging for traditional RF techniques. In MWP, successive temporal differentiation has been shown effective to shape the power spectrum of UWB pulses. The frequency

discriminator chip in Fig. 16 can be programmed to synthesize a first-order and a second-order temporal differentiators simultaneously from both outputs. In this case, UWB pulses coded in the phase of the optical carrier will be converted to variations of pulsed intensity with shaped power spectrum. The experiment setup for the UWB pulse shaping is shown in Fig. 18(a). An example of a result is shown in Fig. 18(b). The top left figure depicts the simulated response synthesized to generate modified UWB doublets. Here, the cascade of drop response from Ring 1 and the through response from Ring 2 was synthesized from Out 1, while the cascade of the through responses from Ring 1 and Ring 3 was obtained from Out 2. The UWB pulses from these outputs, together with their power spectrum, are depicted in Fig. 18(c).

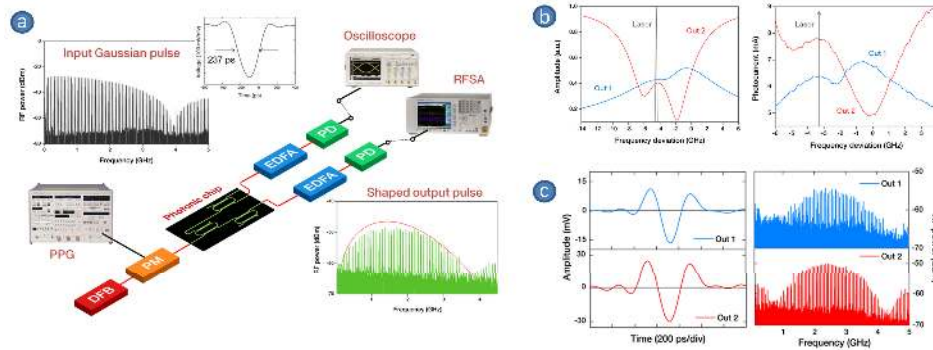


Fig. 18. (a) Schematic of the measurement setup used to demonstrate the pulse shaping. The discriminator chip is configured to shape the Gaussian pulses modulated onto the phase of the optical carrier into a monocycle or a doublet. (b) Simulated (left) and measured (right) ring responses for modified doublet generation. (c) Waveforms (left) and power spectrum (right) of the modified doublets (from [12]).

5.7 Instantaneous frequency measurement

In modern electronic warfare systems, determining the frequency content of a received signal in a quick and accurate manner is of high importance. An instantaneous frequency measurement (IFM) receiver can perform this task. Photonics can be used to enhance IFM systems to achieve large bandwidth. As in previous examples, PM-IM conversion is useful in photonic assisted IFM systems because the frequency information of the received signal can be mapped into the optical intensity, and subsequently, the microwave power. In [13] one of the RRs in the frequency discriminator chip was used to convert PM to IM using both the add and drop responses. The result is an amplitude comparison function (ACF), with which frequency estimation can be achieved. This was the first IFM system with programmable on-chip ACF. The setup of the IFM system is shown in Fig. 19(a), while the ring responses and an example of generated ACF are shown in Fig. 19(b) and 19(c). The ACF was then used to estimate unknown microwave frequencies with low error (Fig. 19(d)).

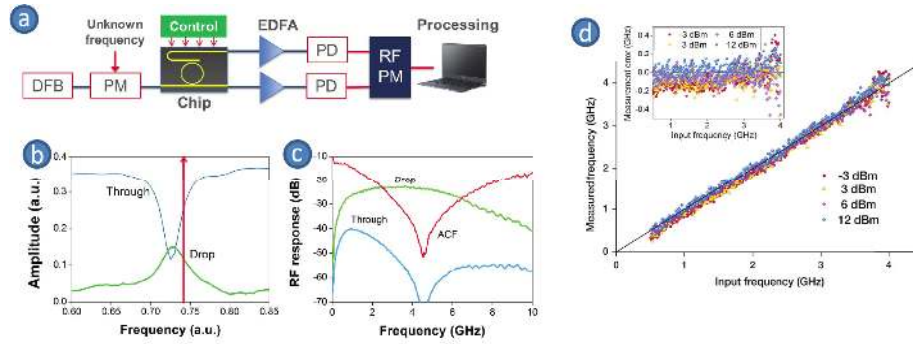


Fig. 19. (a) Schematic of the proposed on-chip IFM system. (b) Measured RR responses, and (c) one of the amplitude comparison functions (ACFs) of the instantaneous frequency measurement (IFM) system. (d) (a) The measured microwave frequency as function of the input frequency for various input power levels, with the frequency error shown in the inset (from [13]).

5.8 Hilbert transformer

Besides being applied as delay lines, another interesting signal processing functionality is the fractional Hilbert transformer (FHT), or in other words, the stand-alone arbitrary phase shift [15]. Similar to the arbitrary phase shifter principle mentioned earlier, a RR as depicted in Fig. 6(a) can provide a tunable phase shift to the RF signals modulated on the optical carrier by making use of its sharp phase transitions around the resonance frequencies and quasi-linear phase responses around the off-resonance frequencies. However, in this case, the optical carrier is always aligned with one resonance frequency of the RR, so that the RR phase response has an anti-symmetric profile with respect to the carrier frequency and therefore allows the regular double-sideband modulated optical signals. Figure 20 depicts the measurements of this FHT functionality of a RR with a FSR of 15 GHz. As it appears, the FHT phase shift can be varied by means of changing the RR coupling coefficient κ . However, a limited phase shift tuning range is exhibited. In practice, this phase tuning range can be linearly extended to 2π by using a cascade of multiple RRs.

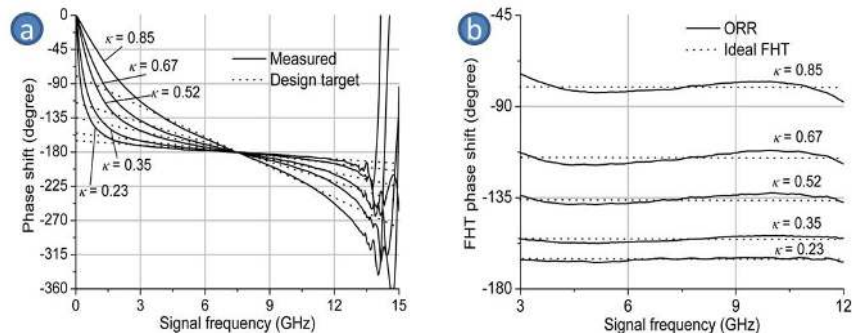


Fig. 20. (a) Measured RF phase response of a waveguide realization of a RR for different values of power coupling coefficient κ and the curve-fittings to the target fractional Hilbert transformer (FHT) specifications; (b) demonstration of the resulting FHT phase shift by removing the delay effect (linear phase) from the measured phase responses (from [15]).

5.9 RF phase control in optical heterodyne-based RF signal generation

The FHT functionality described in the previous section can be applied to the MWP systems for various RF signal processing applications. In addition to this, its photonic implementation also offers an interesting functionality for optical generation of RF signals using optical heterodyne technique. When the two beating optical tones, f_1 and f_2 , are allocated on both

sides of the FHT “phase-jump” frequency (RR resonance frequency) as illustrated in Fig. 21, the FHT phase shift determines the resulting phase of the generated RF signal. The measurements verifying this are depicted in Fig. 22(a). Moreover, this functionality can be further extended to realize a wideband simultaneous I/Q signal generator, using the device architecture shown in Fig. 21. Figure 22(b) depicts the simultaneously generated I/Q RF signals for a frequency range from 7 to 10 GHz, where an RR with an FSR of 15 GHz is used to implement the FHT.

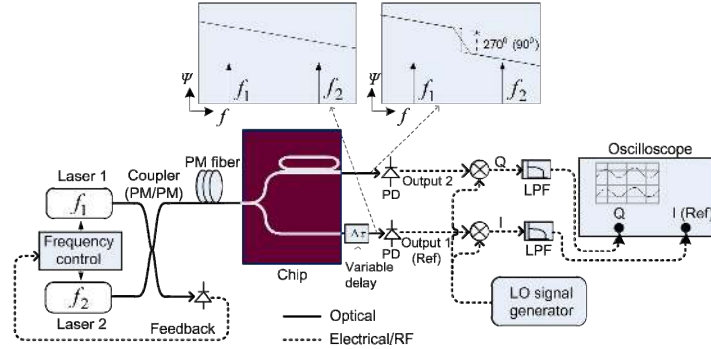


Fig. 21. Setup for experimental demonstration of on-chip phase control of microwave signals generated by optical heterodyning, and simultaneous generation of in-phase and quadrature microwave signals (from [15]).

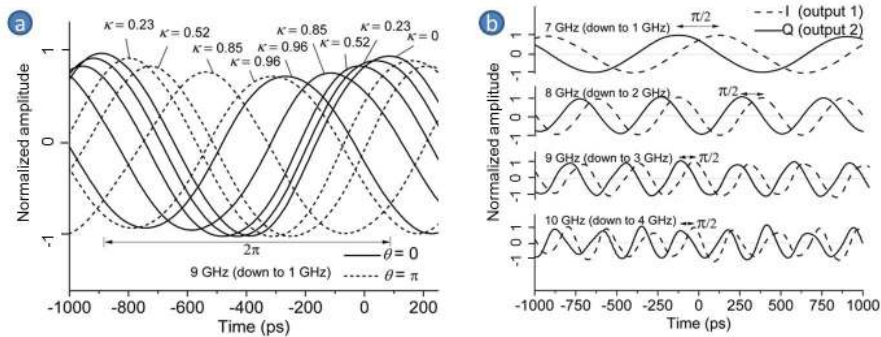


Fig. 22. Demonstrations of two functionalities achieved using the fractional Hilbert transformer (FHT) for optical generation of microwave signals by means of optical heterodyning: (a) microwave phase control with a full 2π phase changing range and (b) simultaneous generation of in-phase and quadrature microwave signals for a wide frequency range (from [15]).

5.10 Microwave polarization network

As described in the previous section, an RR can function as an FHT which includes the case of classic HT, namely a 90-degree phase shifter. This enables the PIC architect of an MZI-double-RR (see Fig. 15(a)) to implement a reconfigurable 2×2 RF coupler [14], which can be switched between two operation modes, namely an in-phase coupler or a hybrid coupler, by means of setting the two RRs independently to the processing status of bypass (decoupling), HT, or a roundtrip-long delay length (full-coupling). In addition to that, the amplitude-tapering and port-switching functionality of the MZI allows a flexible connectivity of the device. One potential application of this reconfigurable 2×2 microwave coupler functionality is a flexible polarization network for dual-linear-polarized antennas. When associated with a coherent optical processing scheme, such a polarization network enables the antennas to transmit or receive simultaneously two orthogonal polarization-multiplexed RF

signals, where both linear and circular polarizations are allowed. An illustration of this is depicted in Fig. 23.

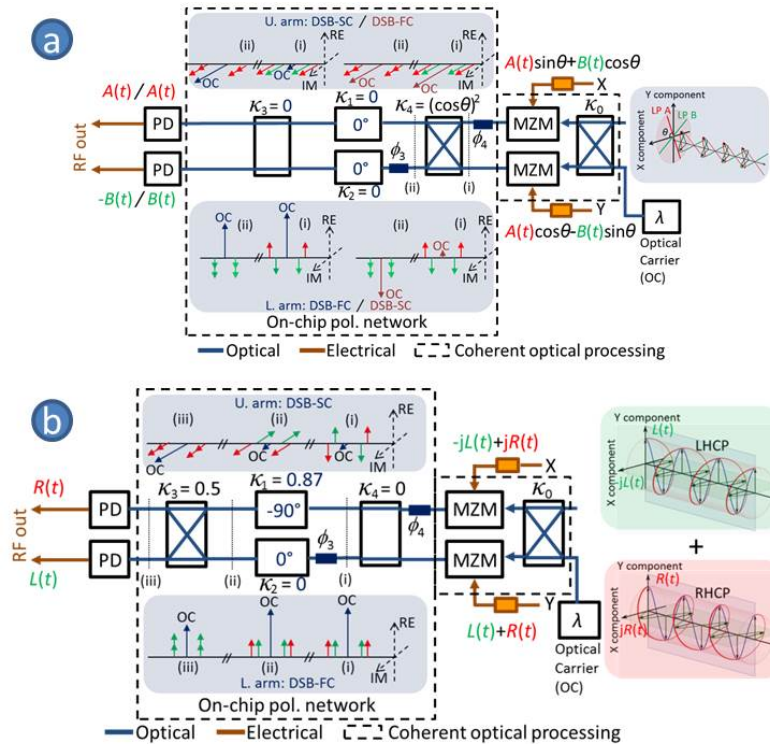


Fig. 23. System schemes for dual-linear-polarization antennas for simultaneous reception of two orthogonal polarization-multiplexed RF signals, using the described MWP polarization network: (a) linear polarization scenario and (b) circular polarization scenario (from [14]).

5.11 Modulation-format transparent MWP signal processors

Another interesting functionality for MWP signal processors is PM to IM converter, which switches the phase-modulated optical signals to intensity-modulated version or vice versa. This functionality can be incorporated in MWP signal processing systems to increase the system flexibility and thereby create new application potentials of MWP signal processors. For example, phase-modulated microwave photonic links may employ this functionality to enable signal recovery using direct detection as an alternative to the approach given in Section 5.2, or direct-modulated lasers may also be used as simple signal sources for PM-based processing systems. An ideal implementation of such a PM-IM converter is an optical all-pass filter with phase response characteristics as illustrated in Fig. 24(a). Here, an abrupt $(2n + 1)\pi$ -phase jump (n is an arbitrary integer) between the optical carrier and one signal sideband causes the modulation format conversion between PM and IM. A practical way to achieve a good approximation of this desired phase response, namely a linear phase response containing an abrupt $(2n + 1)\pi$ -phase jump, is using a waveguide filter consisting of a cascade of RRs. In principle, an ideal lossless RR is a 1st-order all-pass filter and an arbitrary phase response can be approximated by using multiple such RRs in cascade or coupled configurations [16]. In Fig. 24(b), the phase responses of a RR are depicted in contrast to the ideal ones. To verify this concept, a PM signal with modulating frequency sweeping from 10 MHz to 20 GHz was experimentally sent through a TriPleX™ waveguide realization of a cascade of two RRs with a FSR of 25 GHz, and the output of this device was fed to a photodiode to perform direct detection. The measured phase response of the RRs is depicted

in Fig. 24(c), where the two RRs are resonance frequency aligned, exhibiting an improved approximation to the desired response. As depicted in Fig. 24(d), utilizing this phase response for PM-IM conversion, successful signal detection was observed for a bandwidth of 7.5 GHz centered at 12.25 GHz, and this result is achievable for both cases where the optical carrier is aligned to the “left” and “right” phase points, respectively, as indicated in Fig. 23(c).

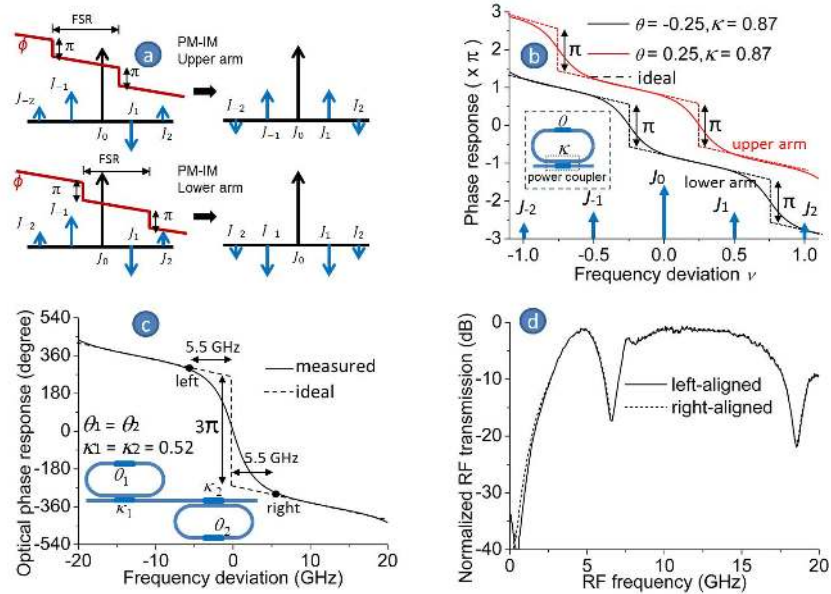


Fig. 24. (a) principle illustration of PM-IM conversion; (b) phase responses of a RR in contrast to the ideal response for PM-IM conversion; (c) measured phase response of a cascade of two RRs; and (d) the measured output RF signals using direct detection after the PM-IM conversion, which are achieved for two cases where the optical carrier is aligned to the “left” and “right” phase points, respectively.

6. Conclusions

In this paper multiple integrated microwave photonic processing functionalities using high contrast silicon nitride (TriPleX™) waveguide technology have been presented. The TriPleX™ technology is especially suited for microwave photonics applications mainly due to the combination of low propagation losses in the optical waveguides and high refractive index contrast between core and cladding, allowing for small bend radii. Consequently, this technology allows for very complex optical circuits to be realized by combining the building blocks on a system level. However, to realize microwave photonic functionalities with ultimate performance, the conversion from RF signals to optical and back requires the active components -such as lasers, modulators and detectors- to be integrated on the platform as well. Despite featuring higher optical propagation losses, InP waveguide technology is prone to provide those active functionalities. Moreover, hybrid integration between InP and TriPleX™ waveguides allows for functionalities using the best of both worlds: active components on InP and low optical propagation loss on TriPleX™. For future work, a schematic of a state of art hybrid-platform solution is shown in Fig. 25, where an InP chip is directly butt-coupled to a TriPleX™ chip. On-chip spot size converters (achieved by tapering waveguides) will ensure low transfer loss between the two platforms, assuming that the waveguides have been aligned properly.

Another important criterion is the total power consumption of the MWP chip which is, in the system depicted in Fig. 25, given by the resistive heater used as tuning elements on the TriPleX™ chip. As example the 16x1 OBFN chip, from Fig. 8 has 120 heaters with an

average total power consumption of 20 W. Alternative tuning solutions, such as those employing liquid crystal claddings, will reduce the total power consumption by many orders of magnitude.

Furthermore, the ongoing effort in on-chip realizations of optical nonlinear effects, such as the frequency comb, four-wave mixing, and etc., tends to open a gateway to various novel on-chip MWP signal processing capabilities. Next to this, the progress in large-scale photonic integration technologies, such as 2-D VECSEL and detector arrays, may also be utilized to largely increase the flexibility and scalability of on-chip MWP systems. All this promises great potentials of broad applications as well as market for on-chip MWP signal processors in the future.

Microwave photonics is a rapidly developing field enabled by advancements in low-loss waveguide and hybrid integration technologies. The enabler to merge these technologies successfully lies within the ability to use optimized technology building blocks which allow creation of on-chip integrated photonic systems and the used packaging and assembly approach. To achieve reliable and robust packaging, developments in industry will play a crucial role. The combination of on-chip manufacturing and automated high-volume assembly and packaging capability will then secure that this technology can be introduced in novel applications at competitive cost levels.

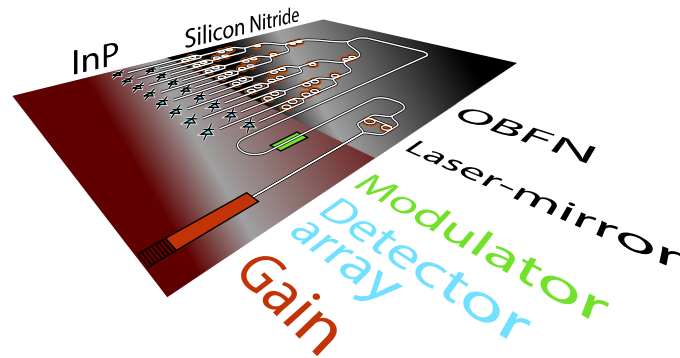


Fig. 25. InP and SiN platform solution for complex microwave photonic processing. Example of an optical beamformer chip for transmit phased array antennas.

Acknowledgment

The research described in this paper is partly funded by the Dutch Point One R&D Innovation Project: Broadband Satellite Communication Services on High-Speed Vehicles, with project number PNE101008, the IOP Photonic Devices Promis2day project IPD12009, and by the European Commission in the 7th Framework Program. The SANDRA project is a Large Scale Integrating Project for the FP7 Topic AAT.2008.4.4.2 (Integrated approach to network centric aircraft communications for global aircraft operations).